



A Physics-informed and data-driven deep learning approach for wave propagation and its scattering characteristics

Soo Young Lee¹ · Choon-Su Park³ · Keonhyeok Park¹ · Hyung Jin Lee² · Seungchul Lee^{1,4,5} 

Received: 18 November 2021 / Accepted: 1 March 2022 / Published online: 9 April 2022
© The Author(s), under exclusive licence to Springer-Verlag London Ltd., part of Springer Nature 2022

Abstract

Understanding the propagation of waves and their scattering characteristics is critical in various scientific and engineering domains. While the majority of present work is based on numerical approaches, their high computational cost and discontinuity in the entire engineering workflow raise the need to resolve obstacles for fully utilizing the methods in an interactive and end-to-end manner. In this study, we propose a deep learning approach that can simulate the wave propagation and scattering phenomena precisely and efficiently. In particular, we present methods of incorporating physics-based knowledge into the deep learning framework to give the learning process strong inductive biases regarding wave propagation and scattering behaviors. We demonstrate that the proposed method can successfully produce physically valid wave field trajectories induced by random scattering objects. We show that the proposed physics-informed strategy exhibits significantly improved prediction results than purely data-driven methods through quantitative and qualitative evaluation from various angles. Subsequently, we assess the computational efficiency of the proposed method as a neural engine, showing that the proposed approach can significantly accelerate the scientific simulation process compared to the numerical method. Our study delivers the potential of the proposed physics-informed approach to be utilized for real-time, accurate, and interactive scientific analyses in a wide variety of engineering and application disciplines.

Keywords Wave propagation · Acoustic scattering · Deep learning · Physics-informed neural networks · Neural simulation

1 Introduction

Understanding wave propagation behaviors and their scattering phenomena has a pivotal role in describing numerous physical processes. Wave scattering demonstrates the reflection of certain objects in relation to the incident waves, thereby explaining the interaction between the objects and

the propagating waves toward them. While there are two main wave scattering problems, i.e., direct and inverse scattering problems, the former characterizes the scattered wave distributions from topological properties of the scattering objects, and the latter uses the observed wave patterns to estimate the objects' properties. Much effort to address these wave scattering problems have provided new opportunities

✉ Hyung Jin Lee
hyungjin.lee@kriss.re.kr

✉ Seungchul Lee
seunglee@postech.ac.kr

Soo Young Lee
leesays92@postech.ac.kr

Choon-Su Park
choonsu.park@kriss.re.kr

Keonhyeok Park
khpark0409@postech.ac.kr

¹ Department of Mechanical Engineering, Pohang University of Science and Technology (POSTECH), 77, Cheongam-ro, Nam-gu, Pohang, Gyeongbuk 37673, Republic of Korea

² Acoustics, Ultrasound, and Vibration Research Group, Korea Research Institute of Standards and Science (KRIS), 267, Gajeong-ro, Yuseong-gu, Daejeon 34113, Republic of Korea

³ Center for Safety Measurements, Korea Research Institute of Standards and Science (KRIS), 267, Gajeong-ro, Yuseong-gu, Daejeon 34113, Republic of Korea

⁴ Institute for Convergence Research and Education in Advanced Technology, Yonsei University, 50, Yonsei-ro, Seodaemun-gu, Seoul 03722, Republic of Korea

⁵ Graduate School of Artificial Intelligence, Pohang University of Science and Technology (POSTECH), 77, Cheongam-ro, Nam-gu, Pohang, Gyeongbuk 37673, Republic of Korea

in a variety of research fields, such as for metamaterial designs with particular functionalities [1–3], non-invasive imaging techniques [4], and interactive sound propagation for virtual and augmented reality environments [5, 6].

While there has been a growing body of methodology for solving the wave-related scattering problems, the majority of the techniques heavily rely on analytical and numerical methods, e.g., finite-element and boundary-element methods [7–11]. Generally speaking, these conventional methods are developed to solve the partial differential equations (PDEs) associated with physically modeled domains. However, the main limitation of the existing approaches is attributed to their excessive computational costs. Computing the wave fields corresponding to each scattering object can take several tens of minutes in practice, hindering the dynamic and immediate realization of the solving process. Furthermore, this constraint not only prevents the method from fulfilling diverse scientific simulations interactively but also disturbs an end-to-end process for various engineering problems, e.g., design optimization, owing to its discontinuous nature for the entire workflow.

To overcome the shortcomings mentioned above, the deep learning (DL) methods have garnered increasing attention for the wave scattering problems. As a data-driven approach, the DL-based method leverages its ability to extract and learn high-level features from data distributions via deeply constructed neural networks, where its direct computation path can be advantageous for efficient evaluation. With the development of various DL algorithms, a couple of studies have been conducted to resolve the wave scattering problems using the DL framework. For instance, Pulkki and Svensson [12] presented a deep neural network-based method to estimate the acoustic scattering effect from the plate-shaped geometry in a source–object–receiver environment. Subsequently, Fan et al. [13] employed a convolutional neural network (CNN) to spatially predict the wave radiation patterns of several simple convex-shaped scatterers given a point source, demonstrating that the evaluation process of the data-driven approach can be faster than the simulation-based computation. Besides, work by Tang et al. [14] suggested a DL approach to estimate the scattered wave fields of 3D geometries using their point cloud representations in a virtual acoustic environment.

Even though previous DL-based approaches have shown plausible results for the wave scattering problems, adopting solely data-driven methods is insufficient in the following circumstances. Developing deep neural network models purely with the dataset is generally a process of fitting an implicit function inherent in high-dimensional data distribution, herein the process is entirely dependent on the training dataset. Through this process, it is obvious that several unseen samples outside the boundary of considered data, e.g., unseen types of scattering objects, can be vulnerable

to the model's generalization under the impossibility of obtaining extremely massive and diverse data for all cases. Furthermore, this simply data-driven approach is likely to provide physically unfeasible results, particularly in certain physical domains where the outcomes should follow recognized rules of physics.

These demands to address the limitations of the data-driven methods have facilitated the advent of the field of physics-informed neural networks (PINNs) [15–17]. The PINNs are designed to incorporate physical knowledge into the data-driven framework by imposing a governing equation on the model's learning process and approximating the results to follow the physics rules. While they have been successfully utilized in several physical domains [18–22], a few pieces of studies using the PINN methods have been introduced for the wave-related problems in the current literature. For example, Karimpouli et al. [23] developed the PINN model using a multi-layered perceptron (MLP) network for solving the 1D seismic wave equation. By directly integrating the physics constraint in the loss function, they showed that the model could precisely estimate the solutions of the seismic wave equation. While Mosely and Markham [24] employed a similar MLP-based approach, the authors investigated the PINN model for solving the acoustic wave equation in the layered velocity domains. Shukla et al. [25] suggested the MLP-based PINN model for characterizing the wave speeds in an ultrasound nondestructive testing application. In addition, several studies have been conducted to obtain the scattered wavefield solutions using the PINN methods. For example, Alkhalifah et al. [26] proposed the PINN method to solve the frequency-domain acoustic wave equation for transversely isotropic media with a vertical axis of symmetry (VTI). The authors proposed the PINN model to obtain the scattered wavefield solutions to avoid point source singularity, where the trained network could serve as a mapping function between spatial coordinates and the complex scattered wavefields. The proposed method was further extended to the following work by Song et al. [27], which evaluated the suggested method extensively from various angles, including model size, solver, and frequency. Though several pioneering works have demonstrated promising results using the PINN framework to solve wave and scattering problems, as the related research is in its infancy, there is considerable room for improving the PINN methodologies for a wide variety of wave and scattering problems.

In this contribution, we propose a deep learning-based method for the wave propagation and scattering characteristics. In particular, we propose the physics-infused deep neural network's architecture and its learning scheme to impose strong inductive biases of wave propagation and scattering-related physics on the data-driven method. By incorporating the wave partial differential equation and boundary conditions into the model's learning process

and structure, respectively, our proposed model is trained to solve the two-dimensional acoustic wave equation in a scattering regime. We analyze the quantitative and qualitative results among the proposed physics-informed method and the comparative methods with only data-driven approaches, from various predictive viewpoints ranging from transient trajectories of wave fields to scattering directivity patterns, and their physical feasibility and consistency analysis. To conclude, we compare the computational powerfulness of our proposed method as a neural engine with the numerical method and convey the potential advantages of our proposed neural method. Our findings suggest the potential applicability of our proposed method for a wide range of wave and scattering-related engineering disciplines.

We structure the remainder of this paper as follows. Our focused problem for wave propagation and scattering analysis is defined in Sect. 2. Section 3 describes the proposed physics-informed method and its evaluation strategies. Section 4 describes and discusses quantitative and qualitative analysis of the comparative methods. Finally, Sect. 5 concludes the paper.

2 Problem statement

We are interested in identifying how different scattering objects induce two-dimensional acoustic wave fields over time steps when a few steps of incident waves and the scattering objects with arbitrary shapes are provided. Figure 1a depicts our focused problem regarding whether the physic-informed DL model can accurately predict the time-dependent roll out trajectories of two-dimensional wave fields as to random scattering object S . The problem is primarily governed by the acoustic wave equation in the form of second-order PDE [28], whose canonical form can be expressed as

$$\left(\nabla^2 - \frac{1}{c^2} \frac{\partial^2}{\partial t^2}\right)P = 0, \tag{1}$$

where c is the sound speed of air ($c=343$ m/s), while ∇^2 indicates the Laplacian operator with respect to two-dimensional Cartesian coordinates. The pressure P is the solution of the equation that describes spatially- and time-varying acoustic wave fields as a function of spatial location (x, y) and time t . The solution of this differential equation satisfies given initial conditions as well as boundary conditions on the scattering object’s reflecting surface S_n .

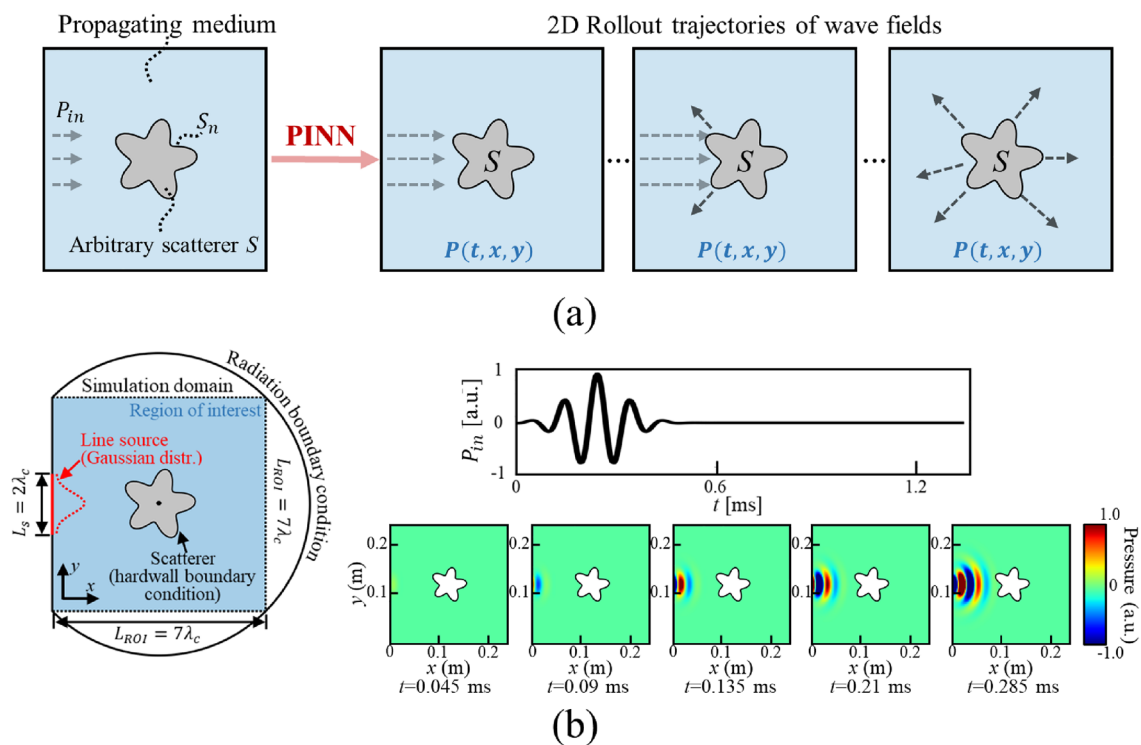


Fig. 1 An overview of the focused scattering problem in two-dimensional acoustic wave propagation medium. **a** A schematic diagram of estimating trajectories of two-dimensional wave fields for an arbitrary

scatterer using a physics-informed neural network (PINN), **b** a description on the problem domain and several examples of input pressure fields considered in this study

Figure 1b shows the overall problem setup considered in this study, consisting mainly of a wave source, a propagating region of interest, and an arbitrary scattering object. First, we consider the wave source to be a modulated Gaussian pulse with a center frequency of 10 kHz. While the source's length L_s is set to be twice the source wavelength λ_c ($=3.43$ cm) at the center frequency, we set the input pressure distribution of the source in the y-axis direction as the Gaussian distribution, as visually indicated by the red dotted line. Regarding the propagating region of interest (ROI), we take into account a squared air medium with a side length of $7\lambda_c$. The considered problem is simulated and solved using the commercial finite element (FE) software, COMSOL Multiphysics. In the simulation, the analysis domain is set up with a circular segment, which includes the ROI. Along the rims of the domain, the radiation boundary condition is employed to minimally reduce unwanted reflection that is not induced by certain scattering object. Since the objects considered throughout this study are sufficiently rigid relative to the background medium air, the hardwall boundary condition is imposed at the scattering object boundaries. Besides, to observe meaningful scattering characteristics according to different inclusion geometries, each scatterer's maximum radius is randomly determined between λ_c and $1.5\lambda_c$. More details on the geometry modeling of the scattering objects and the utilized dataset are described in Sect. 4.1.

Several examples for the simulated wave fields P of scattering objects S are visualized in Fig. 2. First, Fig. 2a describes a sequential wave propagation and scattering process with respect to an example inclusion object, from initial wave incidence to the scattering phenomena and endmost

absorption around the ROI boundaries. As the process progresses, it is possible to observe that the traveling incident waves generate complex scattered patterns as they reach the scattering object and that these induced wave fields later spread over time steps. In this context, it is necessary to predict physically feasible wave fields; for example, the estimated waves should not only not travel further or slower than anticipated, but should also not exhibit spatial characteristics that are physically impossible to occur. On the other hand, Fig. 2b exemplifies representative snapshot wave fields of several scattering objects at the same specific time. This figure implies that the visual representations of wave fields vary depending on the different scattering objects' structures. In this wise, challenges arise in capturing physically valid wave phenomena based on their scatterer-variant topological characteristics, which motivated this study.

3 Physics-informed neural network for wave propagation and scattering characteristics

3.1 Proposed neural network architecture

While our objective can be formulated as the future estimation of two-dimensional wave fields, we propose a deep convolutional neural network (CNN)-based model for spatially predicting the forthcoming wave fields of random scattering objects in a pixel-level manner. Figure 3 describes the overall architecture of the proposed model for wave propagation prediction in a scattering regime. Inspired by the U-net architecture [29], we

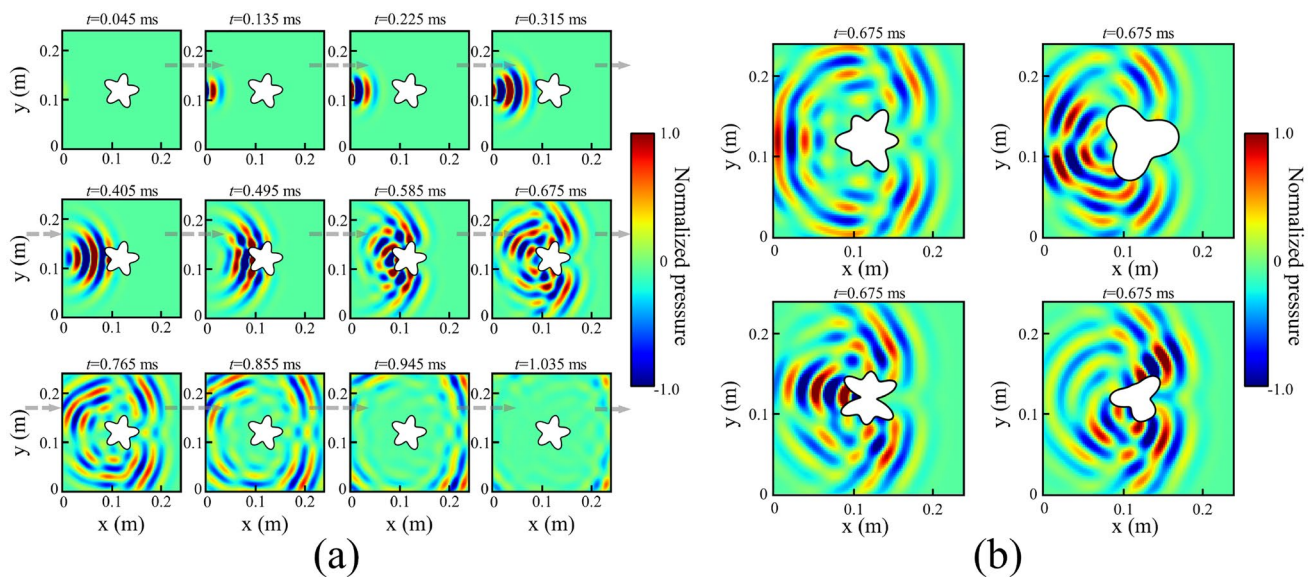


Fig. 2 Examples of simulated wave fields in a scattering regime. **a** Sequential wave propagation and scattering process with respect to a star-shaped scatterer, **b** representative snapshot wave fields of several scattering objects at $t=0.675$ ms

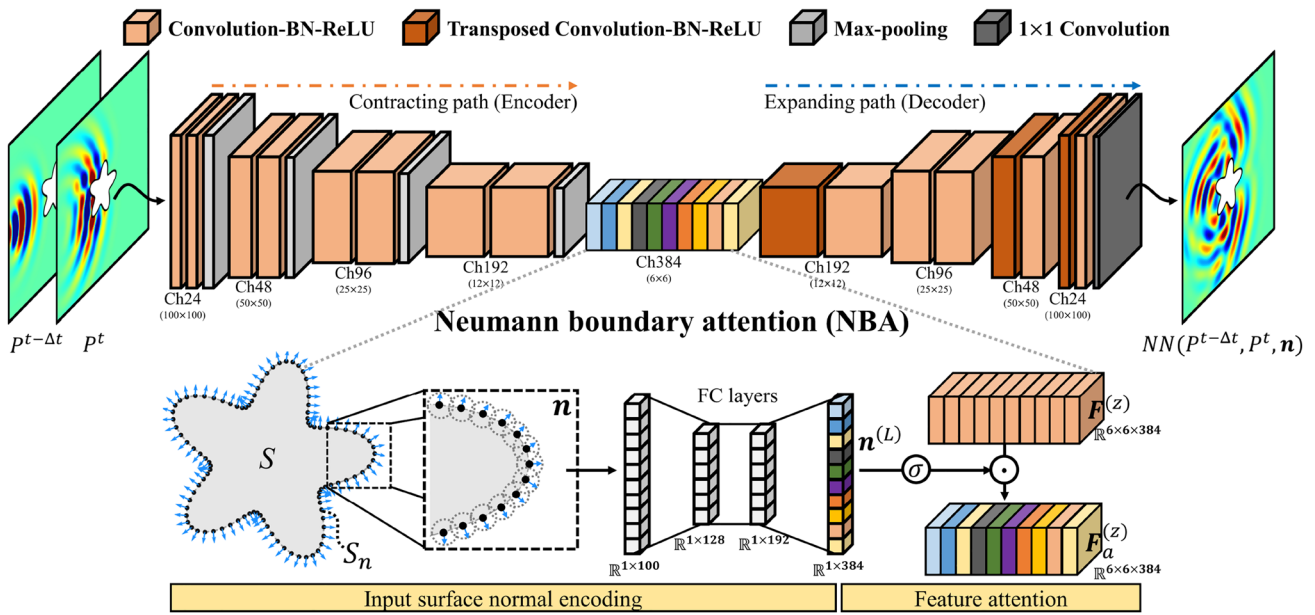


Fig. 3 Proposed neural network architecture to predict sequential trajectories of the two-dimensional wave fields given a certain scattering object

mainly establish a deep convolutional neural network with an encoder–decoder structure as our backbone model. As shown in the figure, the structure of the CNN model is symmetrically constructed with two distinct paths, namely a contracting path and an expanding path. The former path comprises successive two-dimensional convolutional layers to encode higher level spatial feature maps from previous observations of the wave fields for the scattering object S , whilst the latter decoding path takes a role in extracting the enlarged spatial feature maps based on the encoded feature maps to predict the upcoming wave field \hat{P} . Accordingly, the proposed model is trained using pairs of the preceding and subsequent wave fields of various scattering objects in an end-to-end supervised manner.

In particular, we propose a scatterer-noted feature encoding-attending module, denoted as a Neumann boundary attention (NBA), for guiding the boundary condition-informed learning process according to the scattering object’s geometry. As visualized in Fig. 3, the NBA process can be found on latent feature maps in the midst of the entire architecture, where the process consists of two sequential stages: (1) input surface normal encoding and (2) feature attention. First of all, given the scattering object S to predict its wave scattering behaviors, we first extract the scatterer’s unit surface normal information \mathbf{n} by calculating the unit normal vector at each point of the scattering object in a sliding way. The unit normal vector at a certain point (n_{nx}, n_{ny}) can be expressed by the fact that multiplication of the slopes between the perpendicular line and the tangential line equals to -1.

$$(n_{nx}, n_{ny}) = \frac{1}{\sqrt{dx_n^2 + dy_n^2}} (-dy_n, dx_n), \tag{2}$$

where dx_n represents a difference between x components at n -th point and the following point $(x_{n+1} - x_n)$, while dy_n denotes a difference between y components at n th point and the following point $(y_{n+1} - y_n)$. Note that 100 points for the scattering object S are used in this study (Further details are introduced in Sect. 4.1). After calculating the unit normal vectors for every points, we then extract the unit surface normal information \mathbf{n} by converting the unit normal vectors into the direction forms as $\mathbf{n} = \tan^{-1}(\mathbf{n}_{ny}/\mathbf{n}_{nx})$, to represent the unit normal vectors into the scalar values when feeding them into the neural networks. Extracting the unit surface normal information is followed by several fully connected (FC) layers that can be defined as

$$\mathbf{n}^{(l)} = \psi \left(\mathbf{n}^{(l-1)} \mathbf{W}_a^{(l)} + \mathbf{b}_a^{(l)} \right), \tag{3}$$

where $\mathbf{n}^{(l)}$ denotes hidden node values extracted from the l -th FC layer given the input of the unit surface normal information \mathbf{n} , while ψ is a rectified linear unit (ReLU) activation function. Weights $\mathbf{W}_a^{(l)}$ and biases $\mathbf{b}_a^{(l)}$ represent the NBA module’s trainable parameters in the l -th FC layer that should be optimized via training process of the neural network. The consecutive hidden layers of the NBA sub-network are trained to extract high-dimensional features from the unit surface normal information of the scattering object. Subsequently, we adapt the latent feature maps $\mathbf{F}^{(z)}$

extracted from the input wavefields by the encoder networks in the U-Net, using the scatterer's surface normal information encoded from the FC layers $\mathbf{n}^{(L)}$ as follows:

$$\mathbf{F}_a^{(z)} = \sigma(\mathbf{n}^{(L)}) \odot \mathbf{F}^{(z)}, \quad (4)$$

where sigmoid activation σ is considered as the gating operation and \odot represents channel-wise multiplication. By joining the activated output $\sigma(\mathbf{n}^{(L)})$ to the latent feature maps $\mathbf{F}^{(z)}$, we obtain attended feature maps $\mathbf{F}_a^{(z)}$ that contain the scattering object's geometric information. In this way, the high-level information encoded from the scatterer's boundary conditions are trained to capture the appropriate geometric significance and to attend which latent feature maps should be focused on for predicting the upcoming wave fields depending on the scattering object.

3.2 Physics-informed learning scheme

Our strategy for informing the DL framework of wave and scattering knowledge is to design a physics-based multi-part loss function as follows. We design a physics loss criterion \mathcal{L}_p for imposing strong inductive biases regarding the wave and scattering behaviors on the model's learning process, which can be described in view of Eq. (1) and the proposed NBA mechanism as

$$\mathcal{L}_p = \mathcal{L}_{\text{PDE}} + \mathcal{L}_b = \left\| \left(\nabla^2 - \frac{1}{c^2} \frac{\partial^2}{\partial t^2} \right) \hat{P} \right\|_2 + \left\| \frac{\partial P}{\partial \mathbf{n}} - \frac{\partial \hat{P}}{\partial \mathbf{n}} \right\|_2, \quad (5)$$

where \mathcal{L}_{PDE} is minimized in a direction that the predicted wave fields \hat{P} follow the natural wave motions based on the wave partial differential equation. While pixel-level wave fields are considered in this study, we take advantage of the finite difference-based method to extract second-order partial derivatives of the two-dimensional wave fields. On the other hand, the boundary loss \mathcal{L}_b , which describes the Neumann boundary condition of the wave field, is calculated using chain rule-based automatic differentiation of the gradient values within the deep neural network. The \mathcal{L}_b is designed to guide the boundary-conditioning contribution of the proposed NBA mechanism for approximating the wave equation. The model is trained to reduce the difference between $\frac{\partial P}{\partial \mathbf{n}}$ and $\frac{\partial \hat{P}}{\partial \mathbf{n}}$. While simply minimizing the boundary condition term for the predicted wave field, i.e., $\frac{\partial \hat{P}}{\partial \mathbf{n}} \rightarrow 0$, can vanish gradient effect of \mathbf{n} with regard to \hat{P} , we minimize the gap between $\frac{\partial P}{\partial \mathbf{n}}$ and $\frac{\partial \hat{P}}{\partial \mathbf{n}}$ so that the encoded information related to the boundary conditions of the prediction can be approximated to those of the ground truth.

We also take into account the image-based loss function, which is frequently used in data-driven approaches. To

measure the visual similarity of the two-dimensional wave field images, we employ two loss criteria as in the following:

$$\mathcal{L}_v = \mathcal{L}_{\text{MAE}} + (1 - \mathcal{L}_{\text{SSIM}}), \quad (6)$$

where the visual loss function \mathcal{L}_v is combined with the pixel-wise mean absolute error \mathcal{L}_{MAE} and the structural similarity index loss $\mathcal{L}_{\text{SSIM}}$ [30]. While \mathcal{L}_{MAE} determines the pixel-wise distance between the ground-truth and predicted wave fields, $\mathcal{L}_{\text{SSIM}}$ can be used to quantify the spatial and structural resemblance of such wave fields' image patches, ranging from 0 to 1. $\mathcal{L}_{\text{SSIM}}$ can be expressed as

$$\mathcal{L}_{\text{SSIM}}(P, \hat{P}) = \frac{1}{J} \sum_j \frac{(2\mu_{P_j} \mu_{\hat{P}_j})(2\sigma_{P_j, \hat{P}_j})}{(\mu_{P_j}^2 + \mu_{\hat{P}_j}^2)(\sigma_{P_j}^2 + \sigma_{\hat{P}_j}^2)}, \quad (7)$$

where P_j and \hat{P}_j denote the j th 11×11 sliding window patches from the ground-truth wave field P and the predicted wave field \hat{P} . While μ and σ^2 denote local averages and local variances within P_j and \hat{P}_j , σ_{P_j, \hat{P}_j} represents the local covariance between P_j and \hat{P}_j . The $\mathcal{L}_{\text{SSIM}}$ value can be computed by averaging the local SSIM values from the entire windows J . As a higher $\mathcal{L}_{\text{SSIM}}$ value indicates a more visually similar result for the predicted wave field, $(1 - \mathcal{L}_{\text{SSIM}})$ is used to maintain the same loss minimization scheme as the other loss elements.

Lastly, the proposed model is trained based on the combined loss function of the visual loss \mathcal{L}_v and the physics loss \mathcal{L}_p (see Fig. 4). The total loss $\mathcal{L}_{\text{total}}$ can be expressed as

$$\mathcal{L}_{\text{total}} = \left\{ \eta_v \mathcal{L}_{\text{MAE}} + (1 - \eta_v)(1 - \mathcal{L}_{\text{SSIM}}) \right\} + \left\{ \eta_p (\mathcal{L}_{\text{PDE}} + \mathcal{L}_b) \right\}, \quad (8)$$

where η_v and η_p denote parameters that control the significance of the visual loss and the physics loss, respectively, while values of 0.8 and 0.2 are adopted for η_v and η_p in this study. Model training and regularization settings obtained from the random search are summarized as follows. While we utilize AdamOptimizer [31] to optimize the trainable parameters of the proposed model, we apply the mini-batch gradient descent algorithm with a batch size of 60. We also assign the learning rate of $1e-4$, which is reduced depending upon plateaus of the validation loss. Additionally, regularization of the proposed model's training is addressed using a L2 weight decay with its coefficient of $2e-5$ and an early stopping strategy during a total of 300 epochs for the entire training process.

3.3 Evaluation strategies

Based on the proposed neural network architecture and its learning scheme as mentioned above, several comparative models are considered to evaluate the performance of the

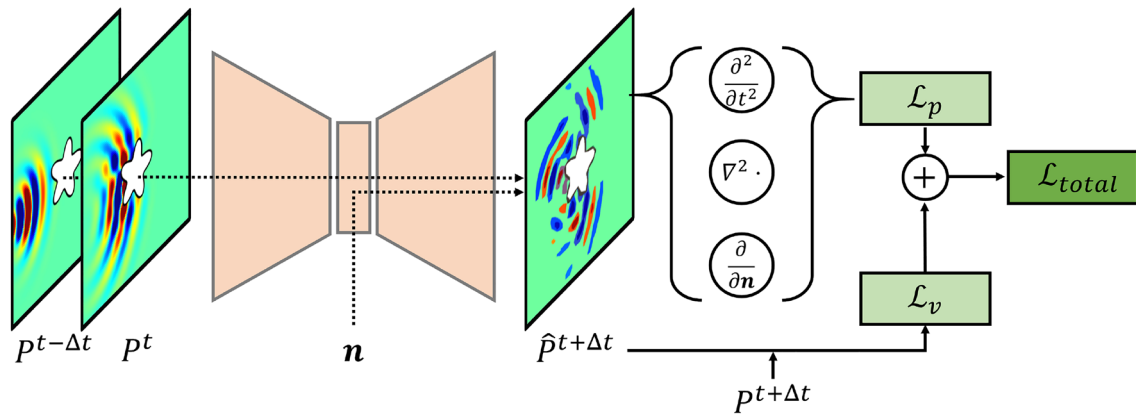


Fig. 4 A schematic diagram for physics-informed learning scheme with combined loss function of the physics loss and the visual loss

proposed physics-informed method. We begin with a naïve u-shaped model (denoted as a baseline) to investigate which extent the simply data-driven model can solve the considered problem. The baseline model with the proposed NBA mechanism (denoted as a baseline+NBA) is also considered to confirm the influence of the boundary condition encoding-attending module under the data-driven framework. Lastly, we evaluate the performance of the proposed model, which incorporates both the NBA mechanism and knowledge-infused learning scheme (denoted as a proposed) to validate the strength and usefulness of such physics-informed method.

We utilize several evaluation metrics to assess the comparative models’ predictive performance for the wave and scattering problem. The evaluation metrics are largely categorized into two groups: image-level and direction-level metrics. As for the image-level metrics, we calculate the image difference between the ground-truth total wave field P and predicted total wave field \hat{P} at each step using mean absolute error (MAE) and 2D-SSIM values. Besides, we consider the direction-level metrics to determine how closely the predicted scattering field’s directional pattern, namely the scattering pattern, matches that of the ground truth. We define the scattering pattern $D_s(\theta)$ as

$$D_s(\theta) = 10 \log_{10} \left[\frac{P_{s,T}^2(\theta)}{\frac{1}{N} \sum_{\theta} P_{s,T}^2(\theta)} \right], \tag{9}$$

where $P_{s,T}$ is the time-averaged absolute map of the scattering field P_s , i.e., $P_{s,T} = \frac{1}{T} \sum_t |P_s^t|$. $P_{s,T}(\theta)$ is defined as a $P_{s,T}$ value extracted from a certain angular point (θ) that is $3\lambda_c$ away from the ROI’s center, where θ resolution is set to be 1° . Accordingly, Eq. (9) represents the scattering directivity pattern normalized by the sum of all directions, where we extract the MAE in dB scale and the R^2 score between the ground truth D_s and the prediction \hat{D}_s .

4 Results and discussion

4.1 Data description

Geometry modeling of the scattering object is considered as follows. To generate a variety of scattering objects with varying geometries, we employ the cosine series-based modeling technique based on the method in [32]. The scatterer modeling technique is conducted by sampling angle-wise coordinates $r(\theta)$ from randomly generated cosine-combined signal and converting them to Cartesian coordinates (x, y) . The angle-wise sampling process can be expressed as

$$r(\theta) = r_0 \left[1 + \sum_i c_i \cos(n_i \theta) \right], \tag{10}$$

where c_i and n_i denote geometric parameters for each basis cosine function, while the three-order formulation of Eq. (10) is adopted in this study. Each value of c_i is randomly determined between -0.35 and 0.35 , and each integer value of n_i is arbitrarily chosen within a range of 2 and 7. θ is set to be uniformly spaced 100 points throughout the angular range of 0 to 2π , and r_0 is randomly selected that the generated scattering object’s maximum radius is placed between λ_c and $1.5\lambda_c$. In addition, as illustrated in Fig. 5a, we consider a random rotation angle ϕ_r to avoid vertical symmetry of the generated object, where ϕ_r is randomly extracted from 0 to π and applied in a counterclockwise direction. As a result, we randomly generate a total of 1000 scattering objects using the above-mentioned process, which are divided into 800 objects for the train set, 50 objects for the validation set, and 150 objects for the test set, respectively. Several examples of the generated scattering objects are visualized in Fig. 5b.

Furthermore, transient wave propagation and scattering phenomena are computed to generate the entire dataset of sequential two-dimensional wave fields from various scattering objects. The wave fields in the simulation domain

Fig. 5 Details on the considered geometry modeling of the scattering object. **a** Random rotation process to avoid vertical symmetry of the generated scattering object, **b** several examples of the generated scattering objects

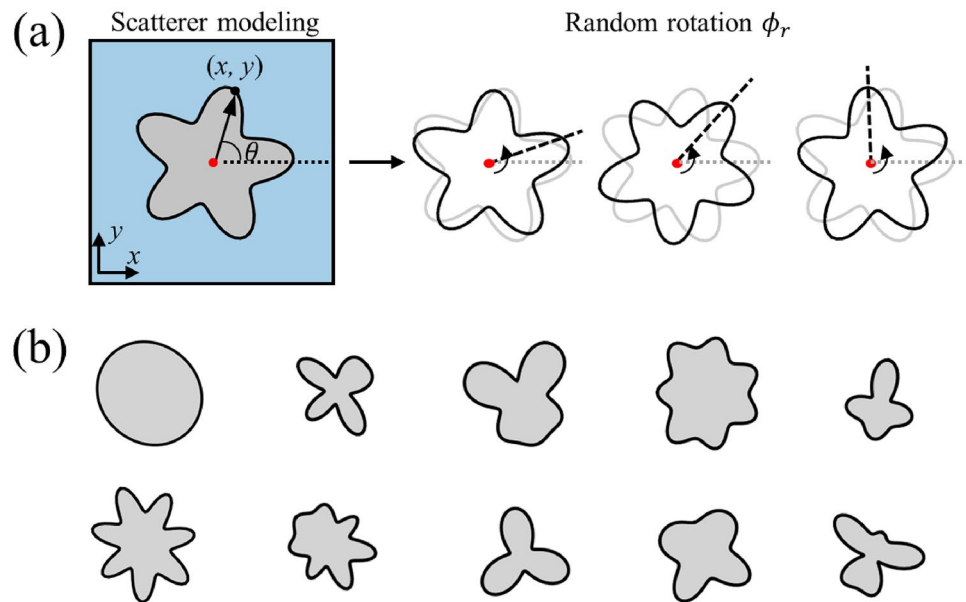


(Fig. 1b) are calculated using time-harmonic finite-element analysis with the commercial software COMSOL Multiphysics, where the transient analysis for each scattering object is conducted to obtain a series of two-dimensional wave fields from wave incidence to propagation, scattering, and absorption around the ROI boundaries. Regarding the spatial dimension of the wave field, 100×100 pressure value extraction points are considered in this study. Besides, the temporal resolution Δt is set to be 0.015 ms, which results in a total of 90 trajectories of two-dimensional wave fields for each scatterer with a total duration of 1.35 ms. Thereafter, the entire dataset is extracted from the sequential wave fields of various scattering objects by sliding a time window of Δt , which means that the dataset comprises multiple pairs of the input sequences ($P^{t-\Delta t}$ and P^t) and the output wave field ($P^{t+\Delta t}$) that are one step ahead of the input sequence. We also apply the min-max normalization between -1 and 1 across the entire dataset to convert the extracted wave fields to a given range and use them for training the proposed model.

4.2 Quantitative analysis

We first evaluate the predictive performance of the comparative models with quantitative results. As introduced in Sect. 3.3, three comparative models, namely a baseline, a baseline with NBA mechanism, and a proposed model, are investigated in our experiments to confirm the effectiveness among simply data-driven and physics-infused approaches for predicting wave propagation and scattering behaviors. To measure each model's difference between the ground-truth wave fields P and predicted wave fields \hat{P} , image-level and direction-level evaluation metrics are used in the

comparative study, where the predicted results are attained from the entire test set.

It should be emphasized that the comparative models' results, i.e., a series of two-dimensional wave field predictions \hat{P} , are extracted not in a snapshot procedure but a *rollout* procedure. The rollout procedure is a method for obtaining a series of wave fields in which the model's predicted output at a specific time step is used as a part of the input sequence in the next step. More specifically, suppose that the transient wave propagation in a scattering regime yields a trajectory of the ground-truth wave fields over K time steps, $P^{t_0:K} = (P^{t_0}, \dots, P^{t_K})$. A *rollout* trajectory of the predicted wave fields can be defined as $\hat{P}^{t_0:K} = (P^{t_0}, P^{t_1}, \hat{P}^{t_2}, \dots, \hat{P}^{t_{K-1}}, \hat{P}^{t_K})$, where the predicted wave field at each time step is iteratively computed by the neural networks NN as $\hat{P}^{t_{k+2}} = NN(\hat{P}^{t_k}, \hat{P}^{t_{k+1}})$. The initial input sequence of wave fields, i.e., (P^{t_0}, P^{t_1}) , can be analytically pre-obtained based on the considered wave source. In this wise, the rollout procedure allows the entire trajectory of the predicted wave fields to be generated via a series of predictions of the neural network model in an iterative manner.

Overall quantitative results among the comparative models are summarized in Fig. 6 and Table 1. First, Fig. 6a presents the comparative analysis of image-level prediction performance using MAE and 2D-SSIM values. As previously stated, MAE and 2D-SSIM measure the degree to which a series of predicted wave fields within the propagating ROI approximate the ground-truth ones, where a lower MAE represents a more accurate pixel-wise pressure value and a higher 2D-SSIM indicates the greater visual similarity of two-dimensional wave fields. As shown in Fig. 6a, it is observed that the baseline model as a way of simply data-driven approach yields the highest predictive errors,

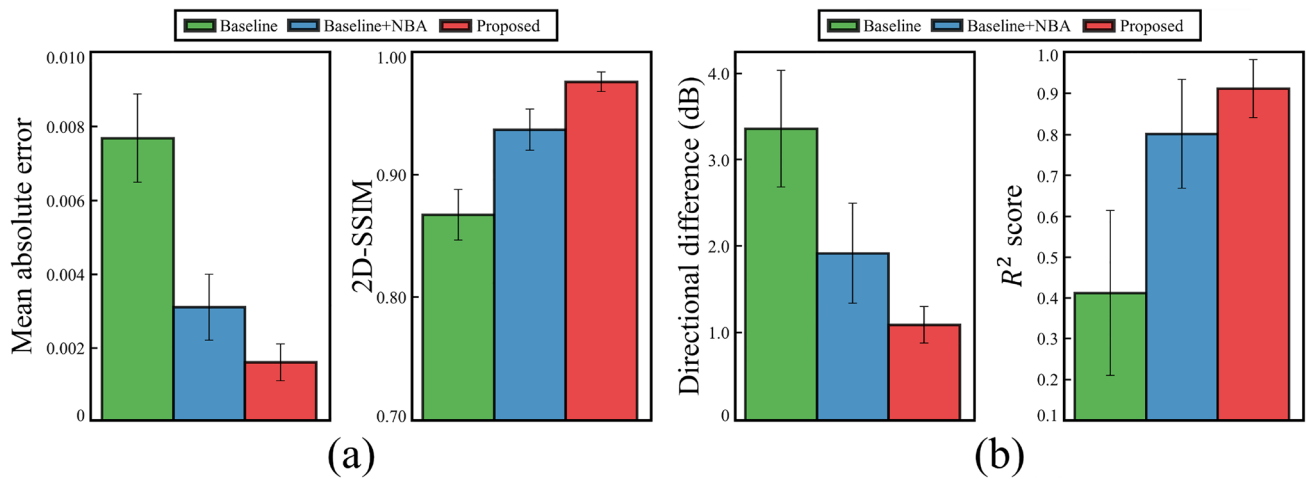


Fig. 6 Quantitative analysis for the comparative models’ prediction performance. **a** Bar charts showing the comparative models’ image-level test results with MAE and 2D-SSIM values, **b** bar charts show-

ing the comparative models’ direction-level test results with directional difference and R^2 score

Table 1 Detailed comparison results for Fig. 6. Each value represents a mean and a standard deviation obtained from the test set

Comparative method	Image-level metrics		Direction-level metrics	
	Mean absolute error	2D-SSIM	Directional difference (dB)	R^2 score
Baseline	0.0077 ± 0.0012	0.8677 ± 0.0207	3.3660 ± 0.6741	0.4177 ± 0.2021
Baseline+NBA	0.0031 ± 0.0009	0.9373 ± 0.0168	1.9286 ± 0.5752	0.8015 ± 0.1333
Proposed	0.0016 ± 0.0005	0.9764 ± 0.0080	1.1022 ± 0.2105	0.9126 ± 0.0712

whereas combining the proposed NBA mechanism into the baseline model improves both MAE and 2D-SSIM results. By extension, we find that our proposed model, which incorporates the physics-informed learning scheme as well as the NBA method, outperforms the other comparative models as to both image-level evaluation metrics, showing an averaged MAE of 0.0016 and an averaged 2D-SSIM of 0.9764, respectively. It is shown that the proposed model exhibits a significant decrease in MAE values and an increase in 2D-SSIM values compared to the other models, indicating that our proposed method can improve the model’s performance for estimating two-dimensional wave fields of unobserved scattering object in the test set.

On the other hand, Fig. 6b delivers the comparative models’ direction-level prediction results, which are used to determine how closely the directional patterns of the predicted wave fields match those of the ground-truth wave fields. As described in Sect. 3.3, after extracting the time-averaged absolute map $\hat{P}_{s,T}$ from the predicted scattering wave fields \hat{P}_s and obtaining the predicted directional pattern $\hat{D}_s(\theta)$ from $\hat{P}_{s,T}$, we locally and globally evaluate the directional similarity between the ground-truth scattering pattern $D_s(\theta)$ and the predicted one $\hat{D}_s(\theta)$ with the angle-wise directional difference and the R^2 score. Similar to the image-level comparison analysis, Fig. 6b indicates that the

proposed model yields the most accurate scattering pattern prediction results among the comparative models. It can be seen that the proposed model produces an averaged directional difference of nearly 1 dB, which is a significant reduction such that one-third compared to the purely data-driven baseline method. Besides, the R^2 score for measuring the distributional resemblance of the scattering pattern is shown to be improved by the proposed method. Notable is the dramatic increase in R^2 score between the baseline and the baseline+NBA, which confirms the advantage of the proposed NBA mechanism for guiding the boundary condition-noted learning process as to the scatterer’s geometry. Along with the proposed NBA module, the proposed method that also capitalizes on the wave and scattering knowledge-infused learning scheme is observed to achieve a more improved R^2 score of 0.9126, showing the highest performance among the comparative models for predicting the scattering patterns.

4.3 Qualitative analysis

We now focus on qualitatively analyzing the wave field predictions obtained from the comparative models. Figure 7 visualizes an example of the predicted wave fields sequentially to assess the comparative models’ prediction

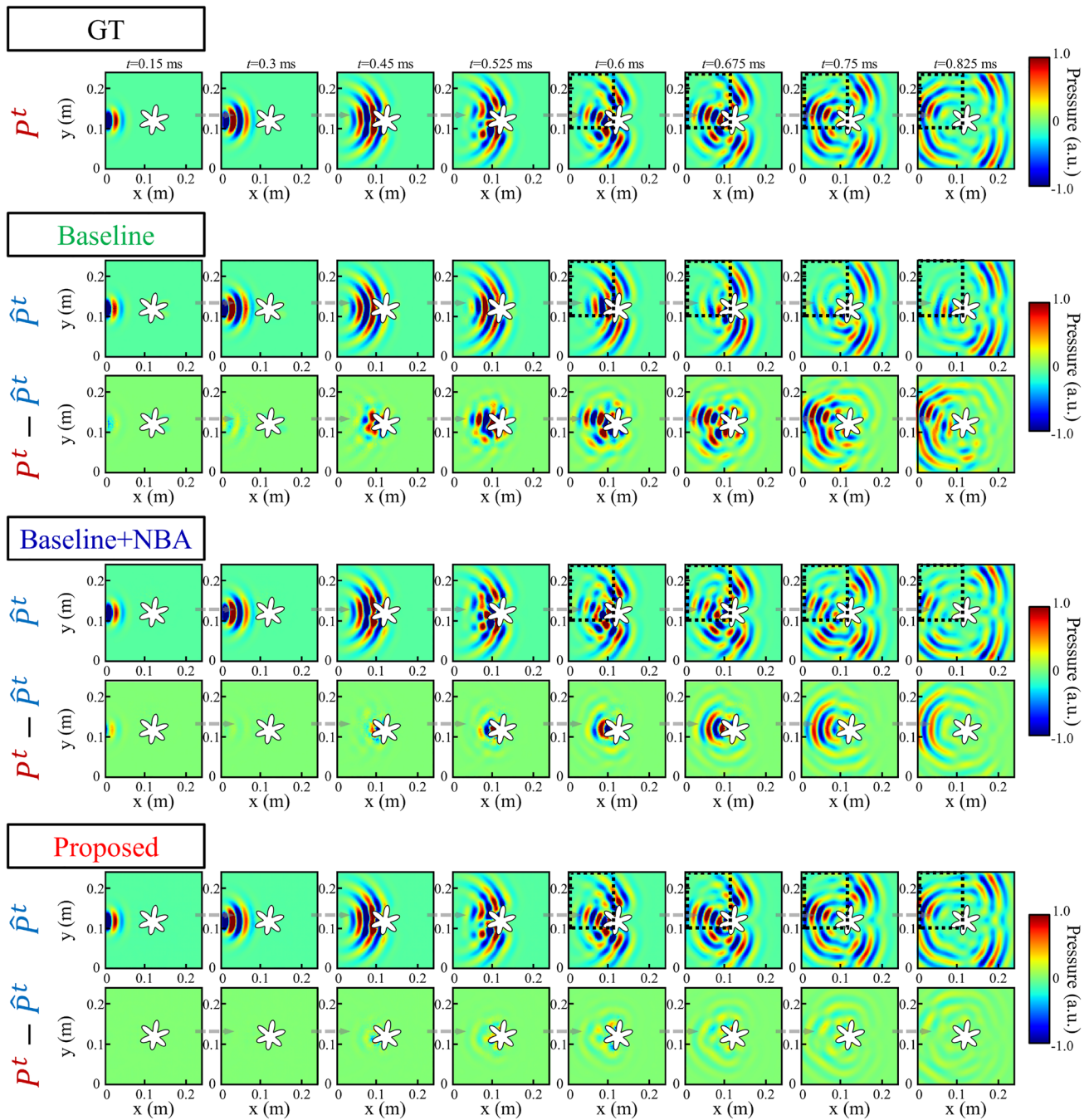


Fig. 7 Comparative prediction results for rollout trajectories of two-dimensional wave fields for an asterisk-shaped scatterer example. Ground-truths P^t , each model’s predicted wave fields \hat{P}^t , and residual

errors $P^t - \hat{P}^t$ are visualized. Each row sequentially represents a subset of wave fields from the whole trajectories

capability for rollout trajectories of two-dimensional wave fields when a certain scattering object is given. While ground truths (GT) P^t , each model’s predicted wave fields \hat{P}^t , and residual errors $P^t - \hat{P}^t$ are depicted with respect to ‘asterisk’-shaped scatterer example in Fig. 7, the results in each column illustrate a subset of the model’s whole prediction trajectories in sequential order. As shown in the figure,

it is observed that the baseline model shows relatively small residual errors in predicting incident wave fields early in the propagation process but exhibits large errors as the waves begin to be scattered. We find that the baseline model fails to capture the scatterer-induced wave directions precisely as well as produces the results that are somewhat inconsistent with natural wave motion characteristics such as traveling

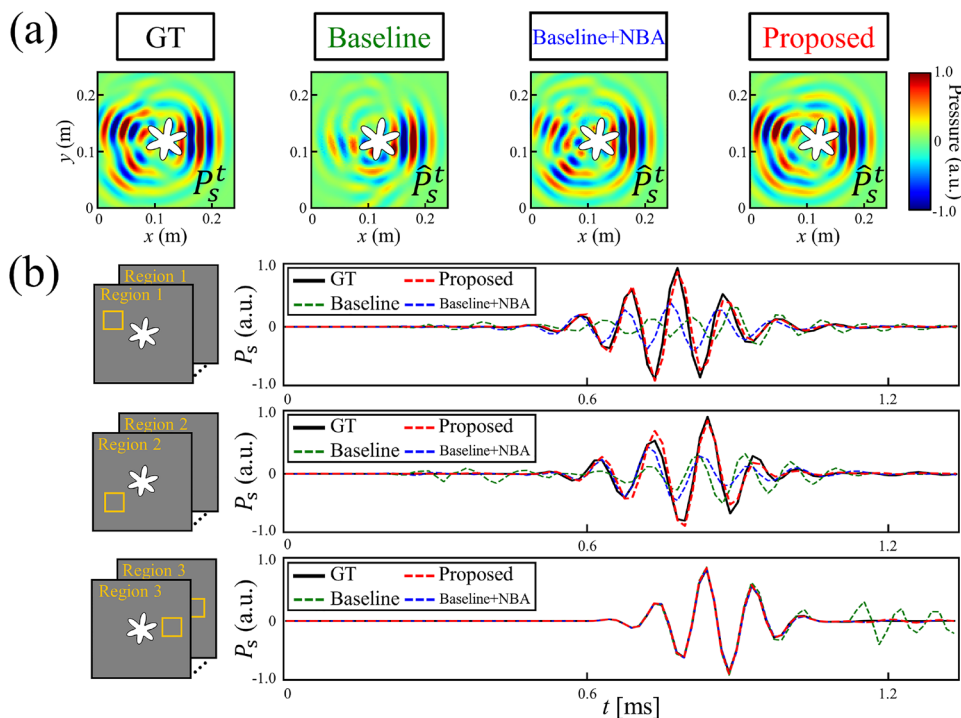
speed and spatial waveform (see dashed boxes in Baseline). Even though the baseline+NBA model predicts the wave field directions better than the baseline to some extent, it is unable to accurately describe wave-like spatial patterns that are similar to the GT, as indicated by the dashed boxes in Baseline+NBA. On the other hand, it can be seen that the proposed model not only accurately predicts the scatterer-induced wave field directions but also generates plausible results that closely match the natural wave field patterns with small residual errors.

Predictive performances of the comparative models are further analyzed from an aspect of scattering field characteristics. Figure 8a shows representative snapshots of the ground-truth scattering field P_s^t and the models' predicted scattering fields \hat{P}_s^t selected from the entire propagation process, where each scattering field can be obtained by subtracting the incident field from the total wave field at each time step. As illustrated in Fig. 8a, one can find that neither the baseline nor the baseline+NBA model performs satisfactorily in scattering field prediction, while the proposed model achieves a plausible result similar to the GT. Additionally, we investigate the scattering wave consistency of the comparative models' results by extracting scattering wave profiles over time steps from different sub-regions (Region 1–3) that contain dominant scattering directions. As shown in Fig. 8b, the baseline and the baseline+NBA model in which physics-based knowledge are not incorporated produce relatively low-quality wave correspondence, as their output do not match the actual wave elements, such as phase and amplitude. On the contrary, it can be seen that the results

of the proposed model nearly coincide with the wave profiles for the three scattering directions. These results are realized by imposing strong inductive biases of the wave and scattering phenomena on the proposed model's training process, enabling the model to learn physically valid behaviors. In this wise, we show that the proposed method outperforms the other methods in predicting the spatial patterns of the wave and scattering as well as satisfying more physically consistent scattering analysis.

We also evaluate the direction-level scattering predictions of the comparative models. To begin, Fig. 9a depicts snapshot images of the GT scattering fields P_s^t and predicted scattering fields \hat{P}_s^t for several scatterer objects, and also time-averaged absolute maps ($P_{s,T}$ and $\hat{P}_{s,T}$) drawn from the entire scattering field trajectories to visually describe dominant directions of the scattered waves during the propagation process. It is shown in Fig. 9a that the purely data-driven baseline model does not adequately capture the scattered wave directions while mispredicting or omitting some of them. On the other hand, we observe that the baseline+NBA begins to capture distinct scatterer-variant directions and that the predicted scattering wave directions can be further elaborated by our proposed method. Additionally, Fig. 9b represents the comparative models' angle-wise scattering directivity results obtained from the $P_{s,T}$ and $\hat{P}_{s,T}$ in Fig. 9a, which also confirms that our proposed method can significantly improve the predictive performance for approximating the ground-truth scattering directivity patterns. As a result, we demonstrate that our proposed method based on the physics-informed framework enhances the performance of the deep

Fig. 8 Comparison analysis regarding scattering field characteristics. **a** Representative snapshot images of the ground-truth and prediction models' scattering fields at $t=0.675$ ms, **b** scattering wave profiles extracted from different sub-regions



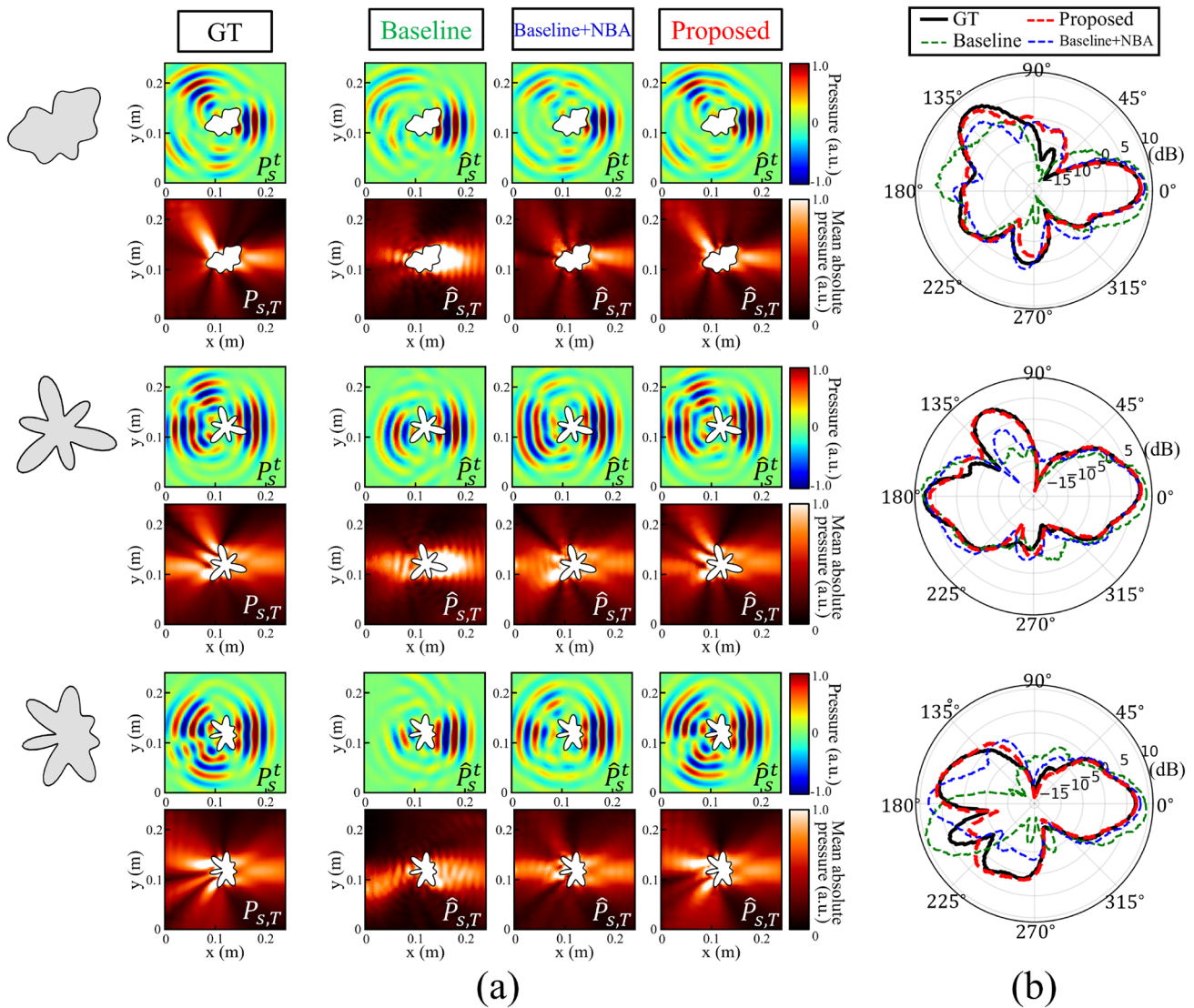


Fig. 9 Qualitative comparison with direction-level scattering patterns. **a** Representative snapshot images of the ground-truth and prediction models' scattering fields (P_s^t vs \hat{P}_s^t) at $t=0.675$ ms and

time-averaged absolute wave field maps ($P_{s,T}$ vs $\hat{P}_{s,T}$), **b** scattering directivity patterns of the ground-truth and predicted results

learning-based approaches for estimating directional patterns of the scattering behaviors as well as sequential wave field trajectories regarding the scatter-varying geometries.

4.4 Extended evaluation

The proposed model is first validated under unseen conditions of varying scatterer sizes and the wave sources with phase delays. To begin, Fig. 10a visualizes the scattering characteristics example of the proposed model according to the different size of scattering object. While the scatterer in the middle is the asterisk-shaped example with the original size considered in this study, the additional examples on the left and right represent the scattering

objects of varying sizes obtained by gradually decreasing or increasing the size by 20% of the original sample. As shown in Fig. 10a, it is observed that the proposed model is capable of capturing the scattering characteristics of several smaller and larger scattering objects that are not considered in the data set. As one can expect, the farther away from the considered original sampling boundary, i.e., the smaller and larger the size, the lower the prediction performance of the proposed model, yet the results are found to be reasonable by achieving a high consistency of scattering fields and their directional patterns. It is worth mentioning that the model could not produce accurate results when the size is too small or large; when the size is too small that evanescent waves are dominant,

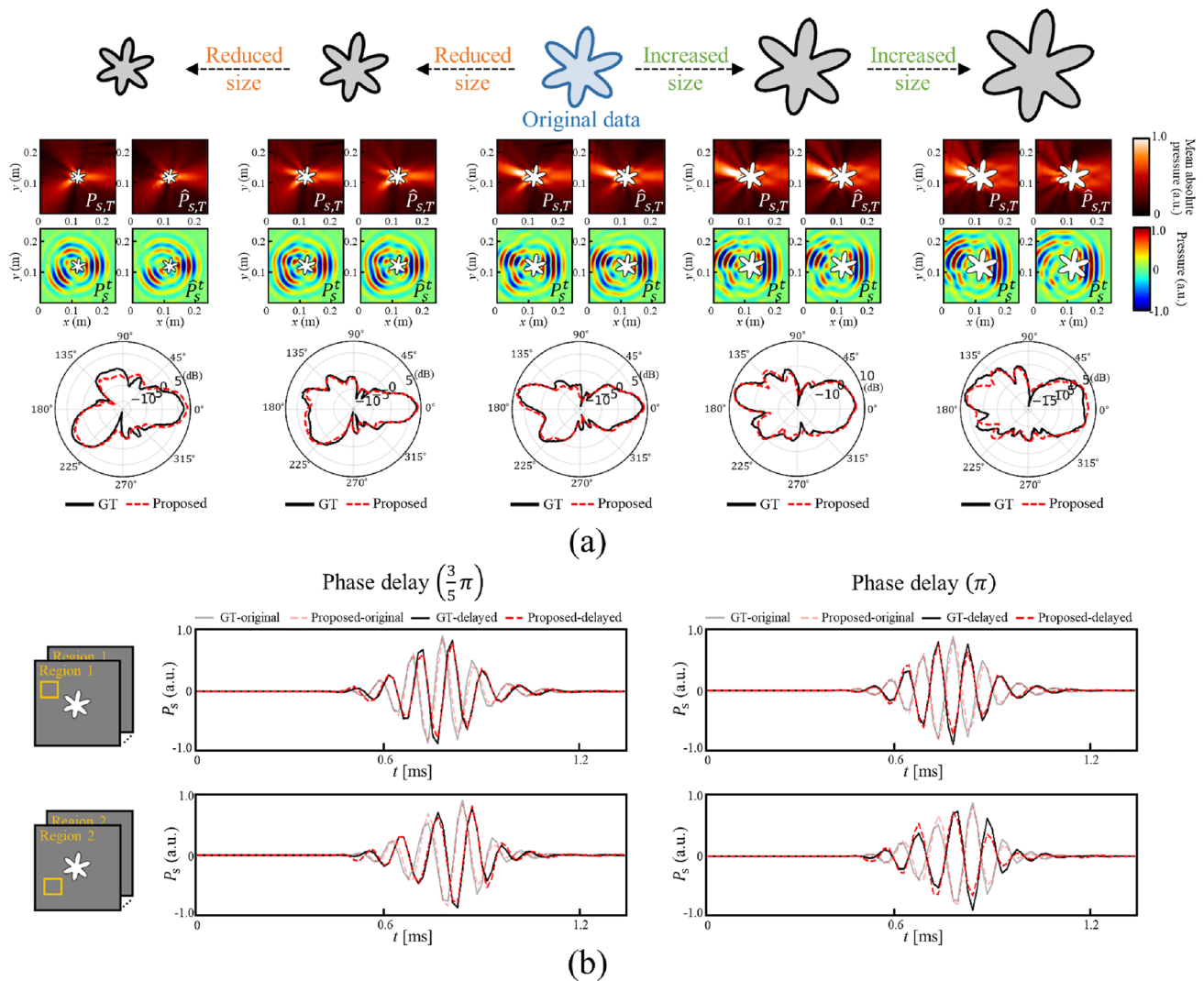


Fig. 10 Prediction performance of the proposed model in terms of unseen conditions. **a** Qualitative examples of the predicted scattering wave fields and scattering directivity patterns for varying scatterer

sizes, **b** qualitative examples of the predicted scattering wave profiles for the wave sources with phase delays

the scattering phenomena are almost similar to those by a point scatterer. On the other hand, when the size was too large, the scattering occurred before reaching the areas where the scattering objects’ hardwall boundaries considered in this study were mainly located. Subsequently, Fig. 10b describes the proposed model’s predicted scattering wave profiles from different sub-regions for the source functions with different phase delays, i.e., $\frac{3}{5}\pi$ and π . While the ground-truth and the predicted scattering wave profiles from the original source function (denoted as GT-original and Proposed original) are overlapped in the background for visual understanding, it can be seen that the prediction results of the proposed model (Proposed-delayed) highly match with the ground-truth ones (GT-delayed) for the phased source functions. As shown in the figure, the

scattering wave profile consistency of the predicted results is guaranteed even when the phase of the input source is opposite.

We now evaluate the predictive performance of comparative models under extended conditions of the scattering object geometries. In this study, additional experiments on extrapolated data set of the scatterer geometries are conducted to compare the models’ results under more topologically diverse situations than the considered data space. We generate the extrapolated test cases by enlarging the sampling ranges of the considered geometry modeling process described in Sect. 4.1: While the four-order formulation of Eq. (10) is considered, each value of c_i and each integer value of n_i are randomly chosen within ranges of $(-0.5\sim 0.5)$ and $(2\sim 10)$, respectively, which are extended ranges relative

to the previously considered ones. Since the enlarged sampling ranges can include the original sampling ranges in a random fashion, we only select the cases if any of c_i and n_i value is outside the original sampling boundary. While 150 samples for the extrapolated test set are generated, Fig. 11a visualizes topological structure distributions of all original scatterers and extrapolated scatterers in two dimensions using t-stochastic neighbor embedding (t-SNE) method [33]. In addition, Fig. 11(b) shows the geometric examples of scattering objects from the original sampling ranges of n_i/c_i , out of the original sampling ranges of n_i/c_i , as well as the extrapolated scatterer that the four-order formulation of Eq. (10) is considered.

Figure 12 shows the comparison results for the extrapolated scattering objects. First, Fig. 12a summarizes both the comparative models' image-level and direction-level prediction differences when assessed with original and extrapolated test data. As shown in Fig. 12a, although the predictive errors of the comparative models generally increase for the extrapolated data, we observe that the proposed model exhibits the lowest degree of performance degradation compared to the other methods. While baseline and baseline+NBA tested with the extrapolated data (denoted as Baseline-Ex and Baseline+NBA-Ex) lead to considerable performance deterioration for both evaluation metrics, it can be seen that the proposed model tested with the extrapolated data (denoted as Proposed-Ex) produces the smallest error increases, showing an averaged pixel-wise MAE of 0.0030 for predicted two-dimensional wave fields and an averaged

angle-wise MAE of 1.64 dB for predicted scattering directivity patterns.

Furthermore, we provide a qualitative example of the models' prediction for scattering characteristics in Fig. 12b. First, scattering wave fields and their directional distributions between the ground-truth and the models' predicted results for the extrapolated scattering object in Fig. 12b show that baseline and baseline+NBA fail to produce accurate prediction results, whereas the proposed model can fairly approximate the actual ground truths. One can find that there exist directional detection errors in the baseline and baseline+NBA model, such as wrongly capturing the directions in which the waves should not be propagated, e.g., a direction nearby 45° in baseline and a direction nearby 110° in baseline+NBA, or ignoring the directions in which the waves should reach, e.g., a direction nearby 225° in baseline and a direction nearby 290° in baseline+NBA. On the other hand, even though the proposed model's predicted directivity pattern differs slightly from the ground truth in some local regions, its predicted scattering directivity reasonably matches the ground truth for the extrapolated scatterer example. In addition, the scattering wave profiles of the comparative models extracted from three different sub-regions are also visualized in Fig. 12b. As shown in the figure, it is observed that the proposed model can achieve the scattering wave profile correspondence for the extrapolated sample, which is in line with our findings in Fig. 8b. On the other hand, it should be noted that the baseline and the baseline+NBA model overall showed more degraded

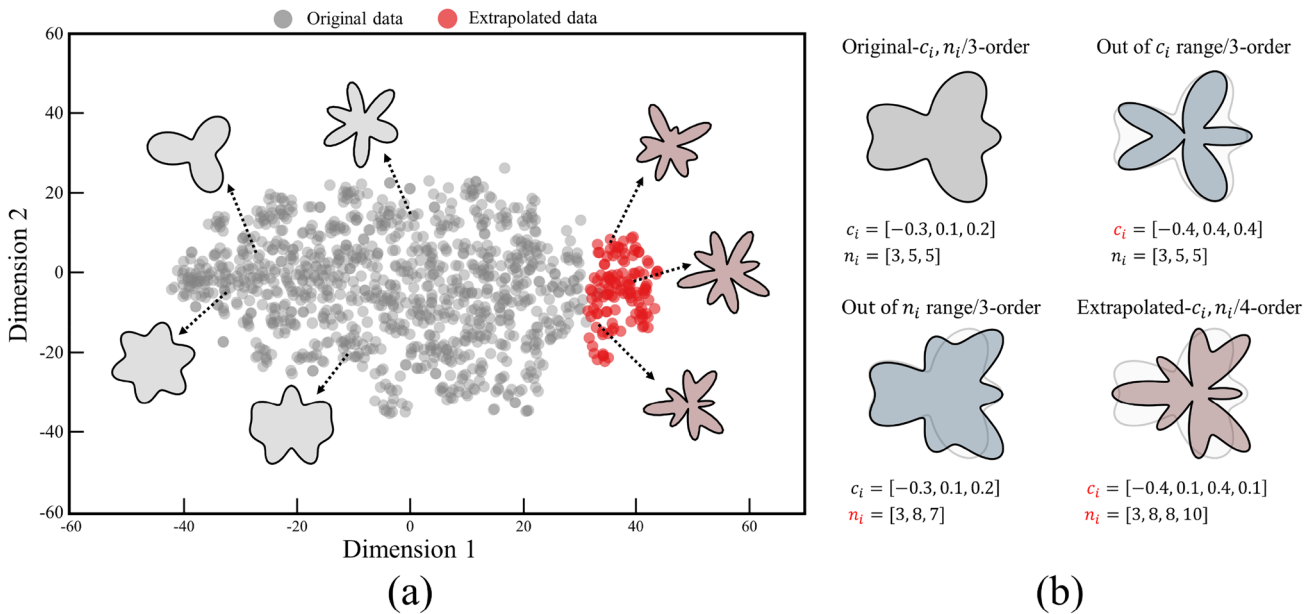


Fig. 11 Description on the original data and the extrapolated data. **a** t-SNE visualization of the original data set and the extrapolated test set, **b** geometric examples of scattering objects from the original sam-

pling ranges of n_i/c_i , out of the original sampling ranges of n_i/c_i , and the extrapolated object with the four-order formulation of Eq. (10)

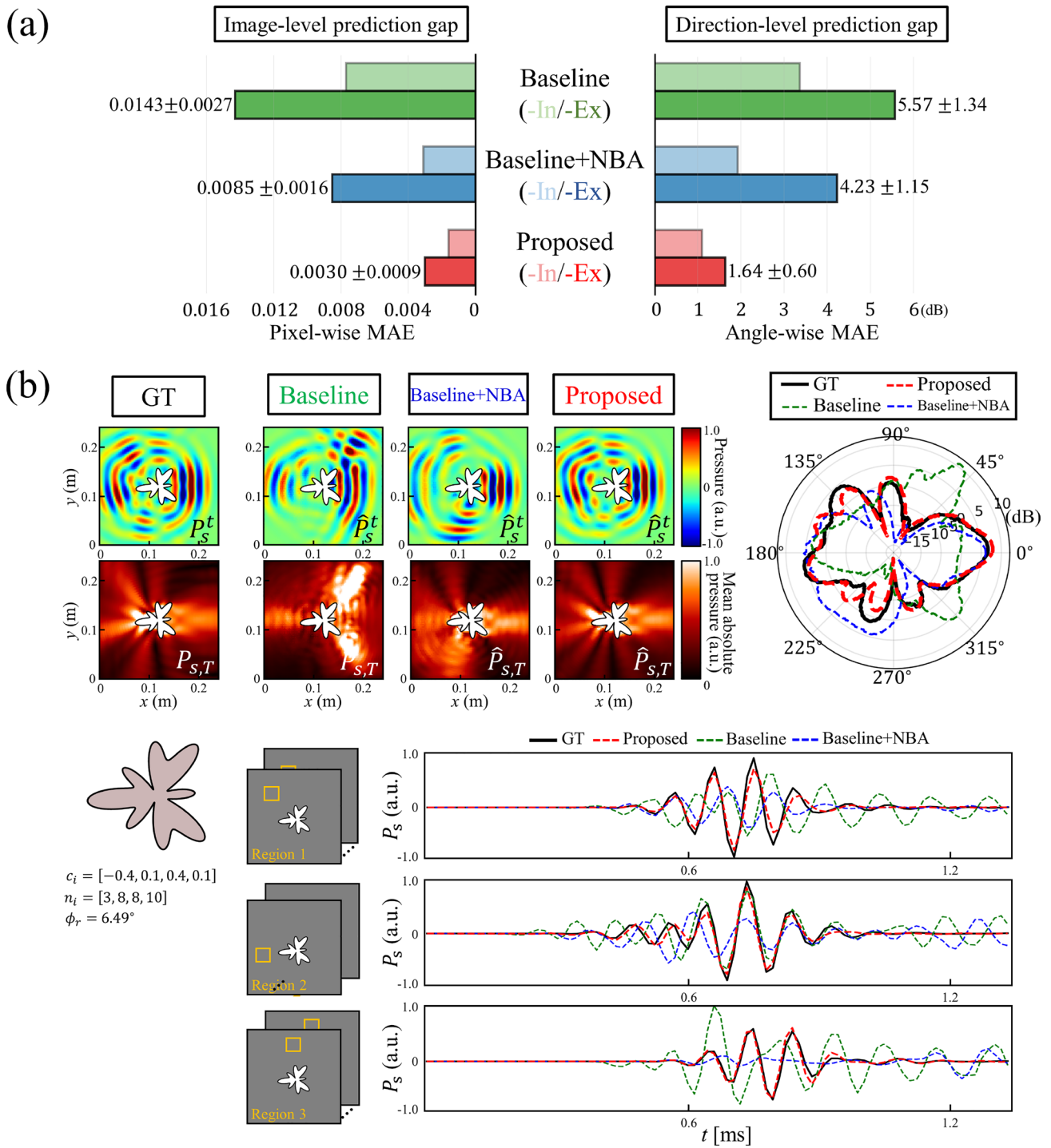


Fig. 12 Prediction performance of the comparative models with respect to the extrapolated test set. **a** Image-level and direction-level prediction gaps when assessed with original and extrapolated test set,

b qualitative example of the models’ prediction comparison in terms of the scattering wave field, directional pattern, and scattering wave profile

results for the extrapolated sample, compared to the scattering object from the original sampling ranges in Fig. 8b.

4.5 Proposed method as a neural engine

Statistical computation time results of the numerical method and the proposed method as a neural engine

are compared to determine the computational efficiency between the two methods, in obtaining certain results for unknown scatterers to analyze for further uses. In terms of the training the network, the proposed neural network model was trained by a NVIDIA GeForce RTX 3090 GPU, which required an average of 214 min and 18 s to complete the training procedure. To evaluate the computational efficiency between the proposed method and the numerical method based on their inference processes, the comparison results are extracted from the entire original test set, while equally using the Intel Core i7-6700 CPU for implementing both methods for comparison purposes. The numerical method using commercial software is shown to be computationally expensive, requiring an average of 85.46 s (± 0.24 s) to complete a transient analysis per a single scattering object. On the other hand, we observe that the proposed method shows significantly lower computation time (0.19 s ± 0.002 s) to predict the transient rollout trajectories of two-dimensional wave fields per a single scatterer, which is approximately 450x faster than the numerical method. We believe that the greater gap in computational efficiency between the numerical and the proposed method can occur when more complex computation tasks are required or when graphics processing units (GPUs) are used to evaluate the results. As a result, this comparison indicates that the proposed method as a neural engine can significantly accelerate scientific and engineering analyses.

We further discuss the potential advantages of the proposed method as a neural engine. Along with its ability to accelerate the solving process, the proposed method can realize more dynamic and interactive analyses. The rapid simulation process of the neural engine can open up new possibilities for interactively addressing and evaluating various engineering problems, such as design optimization and system control. Besides, the enhanced computational efficiency of the neural engine enables the analyzing tool to be more appropriate in embedded and online processing environments. Additionally, this deep neural network-based methodology may enable end-to-end utilization of the gradient-based deep learning scheme for direct and inverse problems. For example, suppose we solve the inverse problem of designing scattering object shapes that exhibit specified scattering patterns via the deep learning framework. In this problem, it is required to verify that the inverse model's results indeed produce the desired scattering patterns using the simulation engine. Here, simultaneous use of an inverse model and a neural simulation engine can improve the continuity of the problem-solving pipeline, which raises the possibility of actively utilizing deep learning-based methods. These potential strengths of the neural engine mentioned above suggest future research directions in a variety of scientific and engineering problems.

5 Conclusion

In this study, we propose a physics-informed deep learning approach for accomplishing fast and accurate problem-solving capability of wave propagation and scattering characteristics. To associate the physical knowledge with the deep learning framework beyond simply data-driven approach, we introduced two strategies to combine strong inductive biases of scatterer boundary conditions and wave equation with the deep neural networks. This approach can expand the model's learning process to a more physically reasonable viewpoint, where the proposed method's prediction is trained to approximate natural physics rules. Both quantitative and qualitative analyses showed that our proposed physics-informed method produced far more accurate results than the purely data-driven methods. Besides, we studied the prediction performance of comparative models under extended conditions of scattering geometries, demonstrating that the proposed method produces the most robust results among the comparative methods. We further examined that the proposed approach as a neural engine could accelerate the problem-solving process 450x faster than the numerical method. Not limited to the wave propagation and scattering-related tasks, we believe that this approach has the potentials to be exploited in a wide range of engineering and application fields that require real-time, accurate, and interactive scientific analyses.

In terms of future research directions, we believe that it is necessary to expand the data space that can describe more diverse conditions of the wave propagation and scattering phenomena, e.g., different scatterer sizes and various source functions, and further to increase versatility of the neural network-based method.

Acknowledgements The research of S.Y.L, K.P, and S.L was supported by the Institute of Civil Military Technology Cooperation funded by the Defense Acquisition Program Administration and Ministry of Trade, Industry and Energy of Korean government under Grant No. 19-CM-GU-01. The research of H.J.L was supported by Enhancement of Measurement Standards and Technologies in Physics funded by Korea Research Institute of Standards and Science (KRISS-2021-GP2021-0002). The authors would like to thank Dr. Wan-Ho Cho, Dr. In-Jee Jung and Dr. Jiho Chang for their helpful discussion concerning experiment and evaluation.

References

1. Kaina N, Lemoult F, Fink M, Lerosey G (2015) Negative refractive index and acoustic superlens from multiple scattering in single negative metamaterials. *Nature* 525(7567):77–81
2. Cai X, Wang L, Zhao Z, Zhao A, Zhang X, Wu T, Chen H (2016) The mechanical and acoustic properties of two-dimensional pentamode metamaterials with different structural parameters. *Appl Phys Lett* 109(13):131904

3. Cummer SA, Christensen J, Alù A (2016) Controlling sound with acoustic metamaterials. *Nat Rev Mater* 1(3):1–13
4. Bertolotti J, Van Putten EG, Blum C, Lagendijk A, Vos WL, Mosk AP (2012) Non-invasive imaging through opaque scattering layers. *Nature* 491(7423):232–234
5. Yeh H, Mehra R, Ren Z, Antani L, Manocha D, Lin M (2013) Wave-ray coupling for interactive sound propagation in large complex scenes. *ACM Trans Graph* 32(6):1–11
6. Mehra R, Rungta A, Golas A, Lin M, Manocha D (2015) Wave: Interactive wave-based sound propagation for virtual environments. *IEEE Trans Vis Comput Graph* 21(4):434–442
7. Watanabe K, Pisanò F, Jeremić B (2017) Discretization effects in the finite element simulation of seismic waves in elastic and elastic-plastic media. *Eng Comput* 33(3):519–545
8. Carrer J, Solheid B, Trevelyan J, Seaid M (2021) A boundary element method formulation based on the caputo derivative for the solution of the diffusion-wave equation. *Eng Anal Bound Elem* 122:1–18
9. Shirron JJ, Giddings TE (2006) A finite element model for acoustic scattering from objects near a fluid–fluid interface. *Comput Methods Appl Mech Engrg* 196(1–3):279–288
10. Yeung C, Ng CT (2019) Time-domain spectral finite element method for analysis of torsional guided waves scattering and mode conversion by cracks in pipes. *Mech Syst Signal Process* 128:305–317
11. Peake M, Trevelyan J, Coates G (2015) Extended isogeometric boundary element method (xibem) for three-dimensional medium-wave acoustic scattering problems. *Comput Methods Appl Mech Engrg* 284:762–780
12. Pulkki V, Svensson UP (2019) Machine-learning-based estimation and rendering of scattering in virtual reality. *J Acoust Soc Am* 145(4):2664–2676
13. Fan Z, Vineet V, Gamper H, Raghuvanshi N (2020) Fast acoustic scattering using convolutional neural networks. In: *IEEE Int. Conf. Acoust. Speech Signal Process*, pp 171–175
14. Tang Z, Meng H-Y, Manocha D (2021) Learning acoustic scattering fields for dynamic interactive sound propagation. In: *IEEE Conf. Virtual Real. 3D User Interfaces*, pp 835–844
15. Karpatne A, Atluri G, Faghmous JH, Steinbach M, Banerjee A, Ganguly A, Shekhar S, Samatova N, Kumar V (2017) Theory-guided data science: a new paradigm for scientific discovery from data. *IEEE Trans Knowl Data Eng* 29(10):2318–2331
16. Raissi M, Perdikaris P, Karniadakis GE (2019) Physics-informed neural networks: a deep learning framework for solving forward and inverse problems involving nonlinear partial differential equations. *J Comput Phys* 378:686–707
17. Arridge S, Maass P, Öktem O, Schönlieb C-B (2019) Solving inverse problems using data-driven models. *Acta Numer* 28:1–174
18. Lihua L (2021) Simulation physics-informed deep neural network by adaptive Adam optimization method to perform a comparative study of the system. *Eng Comput*. <https://doi.org/10.1007/s00366-021-01301-1>
19. Wessels H, Weißenfels C, Wriggers P (2020) The neural particle method—an updated lagrangian physics informed neural network for computational fluid dynamics. *Comput Methods Appl Mech Engrg* 368: 113127
20. Sahli Costabal F, Yang Y, Perdikaris P, Hurtado DE, Kuhl E (2020) Physics-informed neural networks for cardiac activation mapping. *Front Phys* 8:42
21. Sun L, Gao H, Pan S, Wang J-X (2020) Surrogate modeling for fluid flows based on physics-constrained deep learning without simulation data. *Comput Methods Appl Mech Engrg* 361: 112732
22. Goswami S, Anitescu C, Chakraborty S, Rabczuk T (2020) Transfer learning enhanced physics informed neural network for phase-field modeling of fracture. *Theor Appl Fract Mech* 106:102447
23. Karimpouli S, Tahmasebi P (2020) Physics informed machine learning: seismic wave equation. *Geosci Front* 11(6):1993–2001
24. Moseley B, Markham A, Nissen-Meyer T (2020) Solving the wave equation with physics-informed deep learning. *arXiv preprint arXiv:2006.11894*
25. Shukla K, Di Leoni PC, Blackshire J, Sparkman D, Karniadakis GE (2020) Physics-informed neural network for ultrasound nondestructive quantification of surface breaking cracks. *J Nondestruct Eval* 39(3):1–20
26. Alkhalifah T, Song C, bin Waheed U, Hao Q (2021) Wavefield solutions from machine learned functions constrained by the helmholtz equation. *Artif Intell Geosci* 2:11–19
27. Song C, Alkhalifah T, Waheed UB (2021) Solving the frequency-domain acoustic vti wave equation using physics-informed neural networks. *Geophys J Int* 225(2):846–859
28. Morse PM, Ingard KU (1986) *Theoretical acoustics*. Princeton University Press, New Jersey
29. Ronneberger O, Fischer P, Brox T (2015) U-net: convolutional networks for biomedical image segmentation. In: *Int. Conf. Med. Image Comput. -Assist. Interv.*, Springer, pp 234–241
30. Wang Z, Bovik AC, Sheikh HR, Simoncelli EP (2004) Image quality assessment: from error visibility to structural similarity. *IEEE Trans Image Process* 13(4):600–612
31. Kingma DP, Ba J (2014) Adam: a method for stochastic optimization. *arXiv preprint arXiv:1412.6980*
32. Li X, Ning S, Liu Z, Yan Z, Luo C, Zhuang Z (2020) Designing phononic crystal with anticipated band gap through a deep learning based data-driven method. *Comput Methods Appl Mech Engrg* 361:112737
33. Van der Maaten L, Hinton G (2008) Visualizing data using t-sne. *J Mach Learn Res* 9(11):2579–2605

Publisher's Note Springer Nature remains neutral with regard to jurisdictional claims in published maps and institutional affiliations.